Evidence of Nonlinear Coupling in the Edge Harmonic Oscillation Sustaining Quiescent High Confinement in a Tokamak Plasma

R. A. Myers,[1,2,*] J. S. Sarff,[1] B. E. Chapman,[1] K. J. McCollam,[1] M. D. Pandya,[1] R. Xie,[1] Z. Li,[3] D. L. Brower,[4] J. Chen,[4] X. Chen,[3] and W. X. Ding[4]
[1]*University of Wisconsin–Madison, Madison, Wisconsin 53706, USA*
[2]*Oak Ridge Institute for Science and Education, Oak Ridge, Tennessee 37830, USA*
[3]*General Atomics, San Diego, California 92121, USA*
[4]*University of California Los Angeles, Los Angeles, California 90095, USA*

(Received 15 August 2025; revised 26 February 2026; accepted 24 March 2026; published 6 May 2026)

In a tokamak plasma, we measure nonlinear coupling between harmonics comprising a saturated edge oscillation, as predicted by nonlinear magnetohydrodynamic simulations. The coherent structure formed by this coupling suppresses bursty edge-localized modes that cause energy and particle loss. We also measure nonlinear coupling of the edge harmonic oscillation to core-resonant magnetic tearing modes. When tearing modes are present, the edge oscillation harmonics decouple, and edge-localized modes return. We conclude that nonlinear interaction with tearing modes interrupts the formation of the edge harmonic oscillation.

DOI: 10.1103/z7j9-1t1m

Nonlinear three-wave coupling is central to the dynamics of many physical systems. Neutral fluids [1] and both laboratory [2] and astrophysical plasmas [3] are prone to nonlinear wave interactions, affecting transfer of energy and momentum between large and small scales. While this commonly leads to turbulence at a continuum of scales, nonlinear interactions also lead to coherent structures. The formation of large-scale zonal flow, for example, has a profound impact on transport processes, exemplified in the atmospheres of Earth and the gaseous giant planets. Similar structures appear in magnetically confined plasmas and help make fusion conditions accessible [4–6]. Indeed, zonal flow emerges from drift-wave turbulence and forms a transport barrier in the edge region of high-performance tokamak plasmas [7–9]. This causes a spatial steplike increase in the thermal energy profile, which is called the pedestal [10–12]. Strong gradients in the pedestal can cause instability that leads to bursty partial collapses of the transport barrier [called edge-localized modes (ELMs)], expelling heat and particles [13,14]. In ITER and future reactors, large ELMs could damage the nearby vessel wall, so there is a large effort to mitigate their impacts [15]. One active approach is to apply resonant magnetic perturbations that suppress ELMs by relaxing gradients in the pedestal [16].

Spontaneous ELM-free conditions are also observed [17,18]. One important case is QH-mode, where H-mode refers to high confinement associated with the pedestal and Q denotes quiescent, i.e., ELM-free [19]. A key QH-mode dynamic is formation of a 3D coherent structure in the pedestal region. This structure is called the edge harmonic oscillation (EHO), because it contains multiple phase-locked Fourier harmonics with toroidal mode numbers $n = 1, 2, 3, \dots$ (or $n = 2, 4, 6, \dots$), evident especially in magnetic fluctuation measurements [20]. The harmonics have poloidal structure as well. Nonlinear magnetohydrodynamic modeling of QH-mode observed in several tokamak plasmas provides insight on the emergence and role of the EHO [21–27]. ELMing plasmas exhibit a limit cycle bounded by two instabilities: ballooning, driven by plasma pressure, and kink-peeling, driven by plasma current [28–30]. Nonlinear modeling [23,24] inspired by DIII-D tokamak plasmas shows that high-n ballooning modes are linearly unstable and transfer energy nonlinearly to low-n kink-peeling modes, which then saturate. This nonlinear coupling was revealed explicitly in one of these studies using bispectral analysis [23]. Other modeling [25,26] inspired by ASDEX Upgrade tokamak plasmas shows that the longest wavelength kink-peeling modes ($n = 1, 2$) can be linearly unstable and nonlinearly saturate via coupling to higher-n kink-peeling harmonics. In either case, the modeling shows several long-lived, phase-locked kink-peeling harmonics arising that are consistent with the experimentally observed EHO coherent structure. The EHO enhances particle transport across the pedestal, thereby reducing the density gradient, with lesser impact on energy transport and the temperature gradient [19]. Simulations have also been performed for ITER plasmas, suggesting a spontaneous ELM-free reactor plasma is possible if the nonlinear process sustaining the EHO is robust [24]. Nonlinear coupling of pedestal modes does not always lead to

*Contact author: myersr@fusion.gat.com

ELM suppression. Prior investigation of H-mode plasmas exhibiting a substantial delay in ELM onset revealed that nonlinear energy transfer can trigger an ELM [31]. In that case, the pedestal was at the ballooning stability limit. In QH-mode plasmas, the pedestal is sustained away from the ballooning boundary due to the EHO's impact on transport.

In this Letter, we report measurements of the nonlinear coupling between the harmonics forming the EHO during QH-mode in a DIII-D plasma. This provides direct experimental evidence for the nonlinear saturation mechanism that sustains the EHO, as predicted by magnetohydrodynamic modeling [23–26]. We also report experimental evidence that core-resonant tearing modes can nonlinearly interact with the kink-peeling harmonics in the edge. This interaction halts the formation of a long-lived EHO, thereby preventing access to spontaneous ELM-free conditions. Tearing modes are a separate instability related to global gradients in plasma current density or pressure [32–34]. They can trigger major disruptions that cause a sudden, total plasma collapse [35]. In the context of this Letter, the tearing modes appear to interfere with the nonlinear interaction that is key to the formation of the multiharmonic EHO. This implies that sustained QH-mode might require avoidance of EHO coupling to tearing modes. Suppression of tearing modes is a general goal for other considerations like preventing disruptions.

We use interferometry and Faraday-effect polarimetry via the Radial Interferometer-Polarimeter (RIP) diagnostic to measure line-integrated density and radial magnetic field and their fluctuations [36]. RIP includes three horizontally viewing chords at $Z = +13.5, 0, -13.5$ cm, where Z is the vertical distance above or below the equatorial plane. Faraday rotation is proportional to the product of the density and the line-of-sight component of the magnetic field. The line-averaged fluctuating magnetic field is obtained by dividing the fluctuating polarimetry signal by the line-averaged density obtained simultaneously by interferometry. Measurements in this Letter are from the $Z = 0$ chord, yielding the line-averaged fluctuating radial magnetic field $\overline{\delta B_r}$. Since the $Z = 0$ chord is perpendicular to magnetic surfaces (line-of-sight equilibrium $B_r \approx 0$), the density fluctuation contribution to the polarimetry signal is very small relative to $\overline{\delta B_r}$ [36,37].

Magnetic fluctuations are also measured using pickup loop sensors located on the DIII-D vessel wall [38,39]. Away from the resonant surface, tearing fluctuation amplitudes have a characteristic radial decay $\delta B \sim r^{-(m+1)}$, where r is the minor radius and m is the poloidal mode number [40]. Therefore, fluctuations measured by sensing coils may have small amplitude for modes localized in the core region. It has been shown that RIP can detect core-resonant tearing mode onset earlier than sensing coils [37]. Some of the fluctuations involved in the nonlinear interaction described in this Letter are not detected by external sensing coils, because they are core-localized or too small in amplitude. Spatially localized measurements of plasma density fluctuations in the edge are performed via Beam Emission Spectroscopy (BES) [41], which has been used previously to measure EHO structure [42].

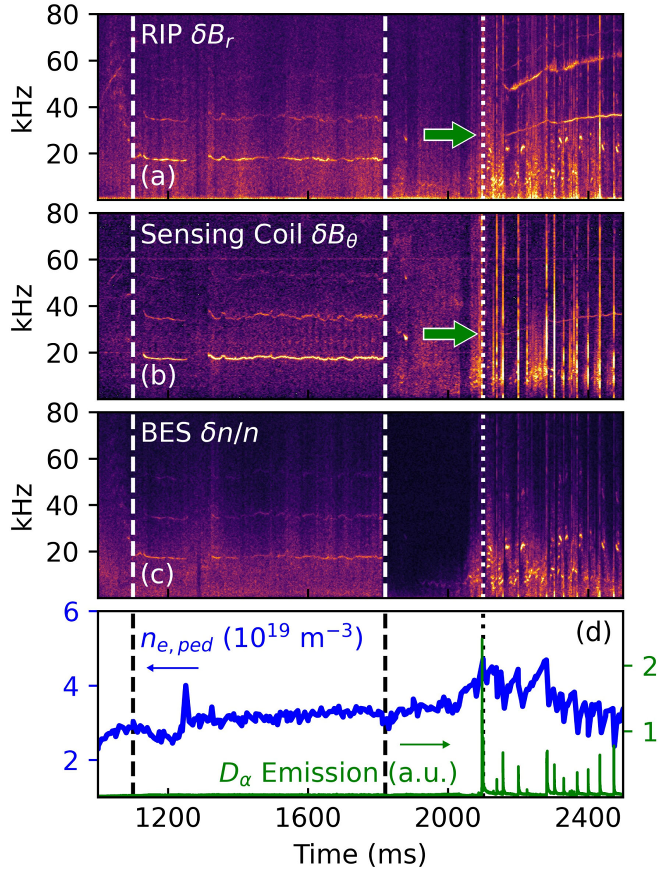

FIG. 1. Data from DIII-D discharge 184791: spectrograms of (a) radial magnetic fluctuations from RIP midplane chord, (b) poloidal magnetic fluctuations from one outboard midplane sensing coil, and (c) density fluctuations from one midplane BES channel near pedestal top. The data sampling rates are 2 MHz for RIP, 0.2 MHz for the sensing coil, and 1 MHz for BES. The geometry of the diagnostics is shown in Fig. 8 in End Matter. Dashed lines denote robust QH-mode. The dotted line marks the onset of ELMy H-mode. Green arrows mark the only mode detected by the sensing coil during the ELMy phase, also detected by RIP. The faint horizontal lines in sensing coil data at 20 and 60 kHz are artifacts. (d) Pedestal electron density n_e and divertor D_α emission.

The analysis described here derives from an example DIII-D discharge (184791) designed to produce QH-mode, with plasma current $I_p = 1.1$ MA, toroidal magnetic field $B_t = 2$ T, and maximum neutral beam heating of 7 MW. Other DIII-D plasmas that enter QH-mode (at least 11 shots in the database that have a robust EHO and the necessary diagnostic complement for the analysis reported here) also exhibit nonlinear coupling within the EHO. All database shots that contained EHO exhibited some coupling between EHO components. Spectrograms of magnetic fluctuations measured by RIP and a low-noise outboard midplane sensing coil are shown in Figs. 1(a) and 1(b). The spectrogram of density fluctuations measured by BES viewing the outboard midplane at normalized minor radial flux coordinate, $\rho = \sqrt{\psi_N} = 0.92$, where ψ_N is the normalized toroidal flux, near the pedestal top is shown in Fig. 1(c). ELM-free QH-mode begins around 1100 ms, marked by a dashed line, when the first three harmonics, around 17, 34, and 51 kHz, of the EHO appear. The EHO fundamental frequency varies gradually in time between 17 and 19 kHz, with second harmonic 34–38 kHz, and third harmonic 51–57 kHz. We henceforth identify each harmonic by its minimum frequency. The toroidal mode numbers of the harmonics are $n = 2, 4, 6$, measured by Fourier analysis of the sensing coil array data. The absence of deuterium-alpha emission (D_α) [43] spikes in Fig. 1(d) in this window indicates lack of ELMs.

QH-mode with a persistent EHO lasts until 1800 ms, when a programmed shape change is imposed, marked by another dashed line. The shape change was intended to be compatible with QH-mode, and controls are held constant afterward. This is followed by a quiet period during which the pedestal density rises, shown by the Thomson scattering [44] data in Fig. 1(d). This implies a reduction in particle transport relative to the earlier EHO period. The density rise is followed by a transition to ELMy H-mode around 2100 ms, marked by a dotted line. Spectrograms of magnetic fluctuations show increased activity after this transition. The vertical stripes are associated with ELMs, also evident in D_α and pedestal density measurements in Fig. 1(d). We interpret the intermittent fluctuation at ≈22 kHz as the EHO attempting to reform. The coherent fluctuations at higher frequency are tearing modes, only one of which (marked with green arrows) is detected by sensing coils.

Nonlinear coupling of modes with frequencies f_1, f_2, and f_3 can occur when frequency matching, $f_1 + f_2 = f_3$, and wave vector matching, $\mathbf{k}_1 + \mathbf{k}_2 = \mathbf{k}_3$, conditions are satisfied. Bispectral analysis is a statistical method that is effective in identifying and quantifying such three-wave interactions in data [2,45,46]. The bicoherence b^2 is a normalization of the bispectrum that measures the degree of nonlinear phase correlation,

$$b^2 = \frac{|\langle X(f_1)Y(f_2)Z^*(f_1+f_2)\rangle|^2}{\langle |X(f_1)Y(f_2)|^2\rangle\langle |Z(f_1+f_2)|^2\rangle}. \qquad (1)$$

Here, $X(f)$, $Y(f)$, and $Z(f)$ are the Fourier transforms of time-series signals, and angle brackets $\langle\rangle$ signify an ensemble average of many sample realizations. Bicoherence analysis can be performed using time-series data from a single signal source ($X = Y = Z$), then called the autobicoherence. When two or three independent signals are used, it is called the cross-bicoherence. If $b^2 = 1$, then all of the fluctuation amplitude at f_3 is phase locked to fluctuations at f_1 and f_2. For $0 < b^2 < 1$, a

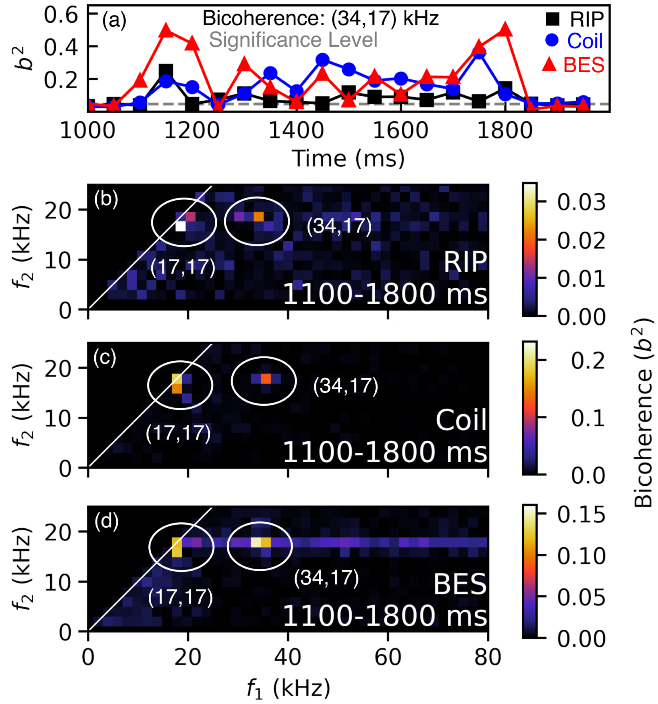

FIG. 2. From data in Fig. 1: (a) evolution of bicoherence for (black squares) RIP, (blue circles) sensing coil, and (red triangles) BES data at the EHO fundamental and harmonic frequencies. The gray dashed line is the 99% significance level. Labeling (f_1, f_2) represents $f_3 = f_1 + f_2$. Averaged from 1100–1800 ms, bicoherence in data from (b) RIP, (c) sensing coil, and (d) BES midplane $\rho = 0.92$. The bispectrum is symmetric across $y = x$ and $y = -x$, so only the $f_2 < f_1$ region bounded by white diagonal lines is populated. The f_2 axis is truncated to focus attention on the peak bicoherences (circled). Row $f_2 = 0$ is suppressed to remove numerical artifacts. Full-frequency-range plots are shown in Figs. 5–7 in End Matter.

proportional fraction of the fluctuation at f_3 is nonlinearly coupled to f_1 and f_2. For an ensemble with sample size N, the auto- or cross-bicoherence is statistically significant if it exceeds $b^2 > 9.2/(2N)$, which is the 99% significance level for a chi-square distribution with a true value of zero in the limit of many degrees of freedom [47–49]. In the previously discussed nonlinear simulations of QH-mode plasmas, the summed bicoherence between EHO harmonics increased between the linear growth and nonlinear saturation phases, an indication that their nonlinear coupling strengthened. The bicoherence spectrum peak also moved to lower n during the nonlinear phase [23].

We measure experimentally the nonlinear coupling between the three lowest-n harmonics of the EHO using bicoherence analysis. In the discussion that follows, the frequency pair (f_1,f_2) represents coupling $f_3 = f_1 + f_2$. Figure 2(a) shows the evolution of the bicoherence between the EHO fundamental and the harmonics at (34,17) kHz, calculated from successive 50 ms periods of RIP, sensing coil, and BES data. Each 50 ms period represents an ensemble of 100 time segments of length 0.5 ms. The 99% significance level for an ensemble average of 100 segments is 0.046, indicated with a gray dashed line. The bicoherence is significant when the EHO is present until it dissipates, consistent with the nonlinear modeling described earlier. The temporal variation suggests that the strength of the nonlinear coupling is dynamic, but variable background noise is likely important as well.

The bicoherence for each possible coupling (f_1, f_2) averaged over the full duration of the QH-mode period of RIP data is shown in Fig. 2(b). The ensemble contains 1400 time segments of length 0.5 ms. Bicoherence for the (34,17) kHz pair is 0.022 in RIP data, 0.13 in sensing coil data, and 0.16 in BES data, each above the 99% significance level of 0.0033. This identifies the persistent nonlinear coupling of the fundamental to its harmonics. Analysis with varied sample size N, shown in Fig. 9 in End Matter, demonstrates statistical convergence of the bispectra. The EHO harmonics are coupled throughout the QH-mode period, but the bicoherence has low magnitude ($b^2 \ll 1$), suggesting the nonlinear coupling may not be very robust.

A persistent EHO is absent when the plasma transitions to ELMy H-mode around 2100 ms, shown with a dotted line in Fig. 1. There is instead an intermittent mode, rising in amplitude a consistent 5–10 ms after each ELM and lasting about 10 ms. The intermittent mode's frequency ≈22 kHz is near the previous EHO fundamental frequency, suggesting this is an EHO attempting to reform. We focus on the first instance of the intermittent mode, which appears at 2164–2175 ms, detailed in Fig. 3. The spectrogram in Fig. 3(a) reveals a second harmonic at 44 kHz, but a third harmonic is not clear. The bright-band fluctuation around 28 kHz is visible in both RIP and sensing coil data. Fourier mode analysis from the sensing coil arrays identifies this to be an $n = 2$ tearing mode with poloidal mode number $m = 3$.

Importantly, other magnetic fluctuations appear only in RIP data. Those dynamically important in what follows are a larger one at 48 kHz and a smaller one at 70 kHz, marked by arrows. There are corresponding density fluctuations at 28, 48, and 70 kHz observed in CO_2 interferometry data [50] that imply the resonant surfaces corresponding to these modes lie in the ranges $\rho = 0.30$–0.41, $\rho = 0.16$–0.30, and $\rho = 0$–0.16, respectively, consistent with all three being core-resonant tearing modes. There are no corresponding BES density fluctuations in the edge region associated with these core-resonant tearing modes.

Amplitudes of the 22 (presumed EHO), 48, and 70 kHz modes, calculated using the short-time Fourier transform using 1 ms time windows, are shown in Fig. 3(b) along with electron pedestal density. Growth of the 48 kHz mode while the 22 and 70 kHz mode amplitudes decrease suggests energy transfer between coupled modes. Density pedestal height remains lower when the intermittent mode is large,

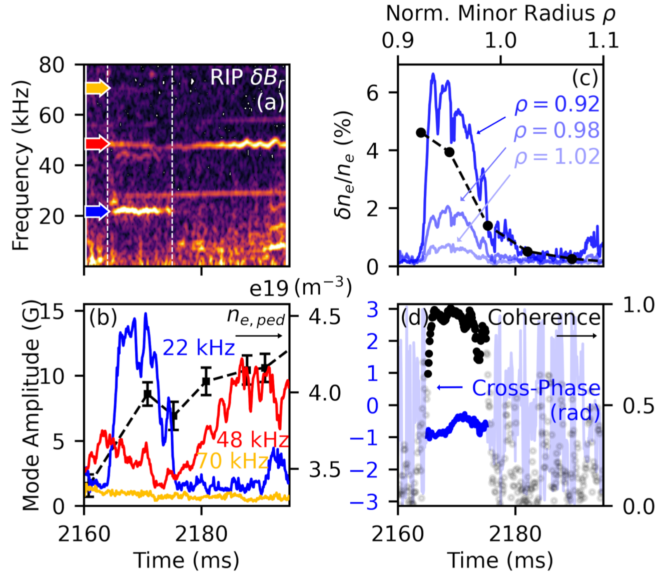

FIG. 3. From the discharge in Fig. 1: (a) spectrogram of RIP $Z = 0$ polarimetry when the EHO reemerges. The blue arrow marks EHO fundamental, the red arrow marks 48 kHz mode, and the yellow arrow marks 70 kHz mode. (b) EHO fundamental (blue), 48 kHz (red), and 70 kHz (yellow) mode amplitudes and electron density pedestal height (black, dashed line). (c) Radial profile of density fluctuation amplitudes at 22 kHz from BES averaged from 2164 to 2175 ms (black circles with dashed connectors) overlaid on the time evolution for the channels at $\rho = 0.92$, 0.98, and 1.02 (blue lines, darkest to lightest). Pedestal top at $\rho = 0.94$, last closed flux surface at $\rho = 1$. (d) Cross-phase (blue) and coherence (black circles) between magnetic fluctuations (RIP) and density fluctuations (BES, $\rho = 0.92$) at 22 kHz. The cross-phase and coherence markings are desaturated where the EHO amplitude is small.

suggesting a transient EHO impact on particle transport. The intermittent mode's 44 kHz harmonic and the 48 and 70 kHz tearing modes are not visible on the sensing coils, emphasizing the importance of RIP data in revealing these dynamics.

While the tearing modes do not appear in density fluctuations in the edge, the intermittent mode at 22 kHz does appear. Figure 3(c) shows normalized density fluctuation amplitudes from power spectra of BES data at 22 kHz, using the short-time Fourier transform with 1 ms time windows as in Fig. 3(b), for three radial locations, $\rho = 0.92$ (near the pedestal top), $\rho = 0.98$, and $\rho = 1.02$ (just past the last closed flux surface). Figure 3(c) also shows in overlay the radial profile of the 22 kHz density fluctuation amplitude from all BES midplane channels averaged from 2164 to 2175 ms. The fluctuation amplitude peaks just inside the pedestal top and decays toward the last closed flux surface. This structure is characteristic of the edge density when an EHO is present [42]. Correlation of internal magnetic fluctuations, measured with RIP, and pedestal density fluctuations, measured with BES, at 22 kHz is shown in Fig. 3(d) to confirm that the same

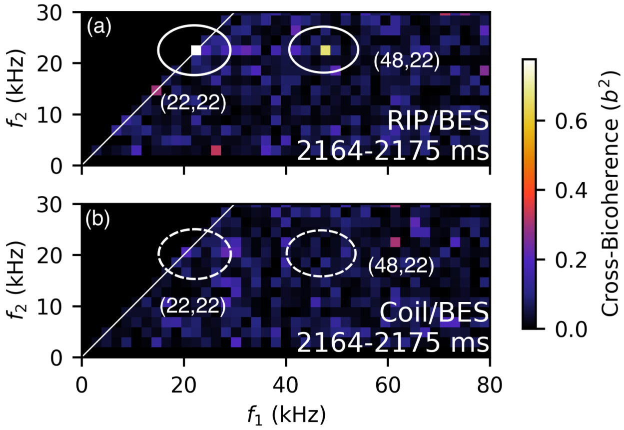

FIG. 4. Cross-bicoherence between (a) RIP and BES and (b) sensing coil and BES data from 2164 to 2175 ms between the vertical dashed lines in Fig. 3(a). The f_2 axes are truncated to focus attention on the bicoherences (circled) involving the modes marked by arrows in Fig. 3(a). Dashed ellipses in (b) highlight absence of bicoherence in BES and sensing coil data.

mode appears on both diagnostics. The well-resolved and stationary cross-phase when the mode amplitude and coherence are large indicates density and magnetic field fluctuations are phase locked, as expected for the EHO.

Nonlinear coupling between the intermittent mode (argued to be a transient EHO) and the tearing modes is revealed by bispectral analysis. The cross-bicoherence spectrum shown in Fig. 4(a) is for an ensemble of BES and RIP data between 2164 and 2175 ms divided into 22 segments of length 0.5 ms. The magnitude of the cross-bicoherence at (48,22) kHz is 0.67, well above the 99% significance level of 0.21. An important difference in the nonlinear dynamics is that there is no significant bicoherence at (44,22) kHz, the frequencies of the transient EHO fundamental and second harmonic. Rather, the fundamental has stronger interaction with the tearing modes. In a torus, wave number matching for nonlinear coupling is $(m_1, n_1) + (m_2, n_2) = (m_3, n_3)$. Given that the EHO fundamental during the 1100–1800 ms period has $n = 2$, the most likely three-wave interaction with the tearing modes is $(n_1, n_2, n_3) = (2, 3, 5)$ or $(2, 4, 6)$, considering the ratio of the mode frequencies (that result from plasma rotation) and the safety factor profile (that determines possible resonant surfaces).

The cross-bicoherence spectrum shown in Fig. 4(b) is for an analogous ensemble of BES and sensing coil data between 2164 and 2175 ms. No significant bicoherence is observed, because the core-resonant tearing modes are not detected in these signals. The RIP diagnostic is vital to reveal nonlinear coupling between the transient EHO and tearing modes, because it is simultaneously sensitive to fluctuations in the edge and core.

In summary, we have detected nonlinear coupling between EHO harmonics in QH-mode, as predicted by nonlinear magnetohydrodynamic modeling [23,24]. To our knowledge, this is the first direct experimental confirmation of the nonlinear coupling process that sustains the EHO, consistent with the assertion from modeling that the EHO saturates through nonlinear phase locking between harmonics. We have also detected nonlinear coupling between core-resonant tearing modes and an intermittent mode that appears to be a transient EHO with characteristics consistent with the persistent EHO seen during QH-mode. One possible physical mechanism for the transient behavior of the EHO in this case could be nonlinear core-edge momentum transport that disrupts the phase locking of EHO harmonics, preventing the formation of a coherent structure and its control of the pedestal density. This would allow ELMs to persist. An implication is that suppression of tearing modes or their coupling might be necessary to attain robust QH-mode with a persistent EHO. This motivates future extensions of magnetohydrodynamic modeling that include QH-mode equilibria, tearing instability, and energy transfer. The RIP diagnostic has been essential to revealing these dynamics, and its further development will help improve understanding of nonlinear coupling in the core and edge. Imposed differential rotation, electron cyclotron current drive, and other control techniques could decouple the core and edge to help make QH-mode viable in future devices like ITER or a fusion pilot plant [51–53].

Acknowledgments—We thank A. Bortolon, K. H. Burrell, G. R. McKee, N. J. Richner, S. D. Stewart, and T. M. Wilks for helpful discussions; B. S. Victor for help with EFIT [54]; and the DIII-D team for enabling this work. This analysis was completed in part using the OMFIT integrated modeling framework [55]. This material is based upon work supported by the U.S. Department of Energy (DOE), Office of Science, Office of Fusion Energy Sciences, using the DIII-D National Fusion Facility, a DOE Office of Science user facility, under Awards No. DE-FC02-04ER54698, No. DE-SC0019003, and No. DE-SC0019004. The first author is grateful for collaboration opportunities enabled by the DOE Office of Science, Office of Workforce Development for Teachers and Scientists, Office of Science Graduate Student Research (SCGSR) program. This research was also supported by the DOE Fusion Energy Sciences Postdoctoral Research Program. Both programs are administered by the Oak Ridge Institute for Science and Education (ORISE) for the DOE under Contract No. DE-SC0014664.

or represents that its use would not infringe privately owned rights. Reference herein to any specific commercial product, process, or service by trade name, trademark, manufacturer, or otherwise does not necessarily constitute or imply its endorsement, recommendation, or favoring by the United States Government or any agency thereof. The views and opinions of authors expressed herein do not necessarily state or reflect those of the United States Government or any agency thereof.

Data availability—The data that support the findings of this article are not publicly available. The data are available from the authors upon reasonable request.

[1] R. H. Kraichnan, Inertial ranges in two-dimensional turbulence, Phys. Fluids **10**, 1417 (1967).

[2] Y. C. Kim and E. J. Powers, Digital bispectral analysis and its applications to nonlinear wave interactions, IEEE Trans. Plasma Sci. **7**, 120 (1979).

[3] A. C.-L. Chian, Nonlinear wave-wave interactions in astrophysical and space plasmas, Astrophys. Space Sci. **242**, 249 (1996).

[4] P. W. Terry, Suppression of turbulence and transport by sheared flow, Rev. Mod. Phys. **72**, 109 (2000).

[5] P. H. Diamond, S.-I. Itoh, K. Itoh, and T. S. Hahm, Zonal flows in plasma-A review, Plasma Phys. Controlled Fusion **47**, R35 (2005).

[6] A. Fujisawa, A review of zonal flow experiments, Nucl. Fusion **49**, 013001 (2008).

[7] C. Holland, G. R. Tynan, R. J. Fonck, G. R. McKee, J. Candy, and R. E. Waltz, Zonal-flow-driven nonlinear energy transfer in experiment and simulation, Phys. Plasmas **14**, 056112 (2007).

[8] M. Xu, G. R. Tynan, P. H. Diamond, P. Manz, C. Holland, N. Fedorczak, S. Chakraborty Thakur, J. H. Yu, K. J. Zhao, J. Q. Dong *et al.*, Frequency-resolved nonlinear turbulent energy transfer into zonal flows in strongly heated L-mode plasmas in the HL-2A tokamak, Phys. Rev. Lett. **108**, 245001 (2012).

[9] G. D. Conway, B. Scott, J. Schirmer, M. Reich, A. Kendl and ASDEX Upgrade Team, Direct measurement of zonal flows and geodesic acoustic mode oscillations in ASDEX Upgrade using Doppler reflectometry, Plasma Phys. Controlled Fusion **47**, 1165 (2005).

[10] L. Schmitz, L. Zeng, T. L. Rhodes, J. C. Hillesheim, E. J. Doyle, R. J. Groebner, W. A. Peebles, K. H. Burrell, and G. Wang, Role of zonal flow predator-prey oscillations in triggering the transition to H-mode confinement, Phys. Rev. Lett. **108**, 155002 (2012).

[11] Z. Yan, G. R. McKee, R. Fonck, P. Gohil, R. J. Groebner, and T. H. Osborne, Observation of the L-H confinement bifurcation triggered by a turbulence-driven shear flow in a tokamak plasma, Phys. Rev. Lett. **112**, 125002 (2014).

[12] I. Cziegler, G. R. Tynan, P. H. Diamond, A. E. Hubbard, J. W. Hughes, J. Irby, and J. L. Terry, Zonal flow production in the L–H transition in Alcator C-Mod, Plasma Phys. Controlled Fusion **56**, 075013 (2014).

[13] F. Wagner *et al.*, Regime of improved confinement and high beta in neutral-beam-heated divertor discharges of the ASDEX tokamak, Phys. Rev. Lett. **49**, 1408 (1982).

[14] M. Keilhacker *et al.*, Confinement studies in L and H-type ASDEX discharges, Plasma Phys. Controlled Fusion **26**, 49 (1984).

[15] A. W. Leonard, A. Herrmann, K. Itami, J. Lingertat, A. Loarte, T. H. Osborne, W. Suttrop, ITER Divertor Physics Expert Group *et al.*, The impact of ELMs on the ITER divertor, J. Nucl. Mater. **266**, 109 (1999).

[16] T. E. Evans, R. A. Moyer, J. G. Watkins, P. Thomas, T. H. Osborne, J. A. Boedo, M. E. Fenstermacher, K. H. Finken, R. J. Groebner, M. Groth *et al.*, Suppression of large edge localized modes in high confinement DIII-D plasmas with a stochastic magnetic boundary, J. Nucl. Mater. **337**, 691 (2005).

[17] M. Greenwald, R. Boivin, P. Bonoli, R. Budny, C. Fiore, J. Goetz, R. Granetz, A. Hubbard, I. Hutchinson, J. Irby *et al.*, Characterization of enhanced Dα high-confinement modes in Alcator C-Mod, Phys. Plasmas **6**, 1943 (1999).

[18] D. G. Whyte, A. E. Hubbard, J. W. Hughes, B. Lipschultz, J. E. Rice, E. S. Marmar, M. Greenwald, I. Cziegler, A. Dominguez, T. Golfinopoulos *et al.*, I-mode: An H-mode energy confinement regime with L-mode particle transport in Alcator C-Mod, Nucl. Fusion **50**, 105005 (2010).

[19] K. H. Burrell *et al.*, Advances in understanding quiescent H-mode plasmas in DIII-D, Phys. Plasmas **12**, 056121 (2005).

[20] K. H. Burrell, M. E. Austin, D. P. Brennan, J. C. DeBoo, E. J. Doyle, C. Fenzi, C. Fuchs, P. Gohil, C. M. Greenfield, R. J. Groebner *et al.*, Quiescent double barrier high-confinement mode plasmas in the DIII-D tokamak, Phys. Plasmas **8**, 2153 (2001).

[21] F. Liu, G. T. A. Huijsmans, A. Loarte, A. M. Garofalo, W. M. Solomon, P. B. Snyder, M. Hoelzl, and L. Zeng, Nonlinear MHD simulations of quiescent H-mode plasmas in DIII-D, Nucl. Fusion **55**, 113002 (2015).

[22] J. R. King, S. E. Kruger, K. H. Burrell, X. Chen, A. M. Garofalo, R. J. Groebner, K. E. J. Olofsson, A. Y. Pankin, and P. B. Snyder, MHD modeling of a DIII-D low-torque QH-mode discharge and comparison to observations, Phys. Plasmas **24**, 055902 (2017).

[23] J. G. Chen, X. Q. Xu, C. H. Ma, P. W. Xi, D. F. Kong, and Y. A. Lei, Impact of $\mathbf{E} \times \mathbf{B}$ shear flow on low-n MHD instabilities, Phys. Plasmas **24**, 050704 (2017).

[24] F. Liu, G. T. A. Huijsmans, A. Loarte, A. M. Garofalo, W. M. Solomon, M. Hoelzl, B. Nkonga, S. Pamela, M. Becoulet, F. Orain, and D. Van Vugt, Nonlinear MHD simulations of QH-mode DIII-D plasmas and implications for ITER high Q scenarios, Plasma Phys. Controlled Fusion **60**, 014039 (2018).

[25] L. Meier, M. Hoelzl, A. Cathey, G. Huijsmans, E. Viezzer, M. Dunne, J. van Dijk, D. J. Cruz Zabala, K. Lackner, S. Günter, MHD simulations of formation, sustainment and loss of quiescent H-mode in the all-tungsten ASDEX Upgrade, Nucl. Fusion **63**, 086026 (2023).

[26] A. Cathey, M. Hoelzl, L. Meier, M. G. Dunne, G. T. A. Huijsmans, L. Gil, G. F. Harrer, N. Aiba, D. J. Cruz-Zabala, K. Lackner *et al.*, Non-linear MHD investigations of high-confinement regimes without type-I ELMs in ASDEX

Upgrade and JT-60SA, Nucl. Fusion **64**, 096003 (2024).

[27] Z. Liang, M. Hoelzl, A. Cathey, D. Hu, S. Y. Dai, Y. L. Liu, D. Z. Wang, and JOREK Team, Predictive nonlinear MHD simulations of quiescent H-mode plasma in the HL-3 tokamak, Phys. Plasmas **32**, 012502 (2025).

[28] ASDEX Team, The H-mode of ASDEX, Nucl. Fusion **29**, 1959 (1989).

[29] J. W. Connor, A review of models for ELMs, Plasma Phys. Controlled Fusion **40**, 191 (1998).

[30] P. B. Snyder, H. R. Wilson, J. R. Ferron, L. L. Lao, A. W. Leonard, T. H. Osborne, A. D. Turnbull, D. Mossessian, M. Murakami, and X. Q. Xu, Edge localized modes and the pedestal: A model based on coupled peeling–ballooning modes, Phys. Plasmas **9**, 2037 (2002).

[31] A. Diallo, J. Dominski, K. Barada, M. Knolker, G. J. Kramer, and G. McKee, Direct observation of nonlinear coupling between pedestal modes leading to the onset of edge localized modes, Phys. Rev. Lett. **121**, 235001 (2018).

[32] H. P. Furth, J. Killeen, and M. N. Rosenbluth, Finite-resistivity instabilities of a sheet pinch, Phys. Fluids **6**, 459 (1963).

[33] H. P. Furth, P. H. Rutherford, and H. Selberg, Tearing mode in the cylindrical tokamak, Phys. Fluids **16**, 1054 (1973).

[34] R. J. La Haye, Neoclassical tearing modes and their control, Phys. Plasmas **13**, 055501 (2006).

[35] P. C. de Vries, M. F. Johnson, B. Alper, P. Buratti, T. C. Hender, H. R. Koslowski, V. Riccardo, and JET-EFDA Contributors, Survey of disruption causes at JET, Nucl. Fusion **51**, 053018 (2011).

[36] J. Chen, W. X. Ding, D. L. Brower, D. Finkenthal, C. Muscatello, D. Taussig, and R. Boivin, Faraday-effect polarimeter diagnostic for internal magnetic field fluctuation measurements in DIII-D, Rev. Sci. Instrum. **87**, 11E108 (2016).

[37] M. D. Pandya, B. E. Chapman, K. J. McCollam, R. A. Myers, J. S. Sarff, B. S. Victor, D. P. Brennan, D. L. Brower, J. Chen, W. X. Ding, C. T. Holcomb, N. C. Logan, and E. J. Strait, Early internal detection of magnetic tearing and implications for tokamak magnetohydrodynamic stability, Phys. Plasmas **31**, 070706 (2024).

[38] E. J. Strait, Magnetic diagnostic system of the DIII-D tokamak, Rev. Sci. Instrum. **77**, 023502 (2006).

[39] J. D. King, E. J. Strait, R. L. Boivin, D. Taussig, M. G. Watkins, J. M. Hanson, N. C. Logan, C. Paz-Soldan, D. C. Pace, D. Shiraki *et al.*, An upgrade of the magnetic diagnostic system of the DIII-D tokamak for non-axisymmetric measurements, Rev. Sci. Instrum. **85**, 083503 (2014).

[40] R. J. La Haye, R. J. Buttery, S. Guenter, G. T. A. Huysmans, M. Maraschek, and H. R. Wilson, Dimensionless scaling of the critical beta for onset of a neoclassical tearing mode, Phys. Plasmas **7**, 3349 (2000).

[41] G. McKee, R. Ashley, R. Durst, R. Fonck, M. Jakubowski, K. Tritz, K. Burrell, C. Greenfield, and J. Robinson, The beam emission spectroscopy diagnostic on the DIII-D tokamak, Rev. Sci. Instrum. **70**, 913 (1999).

[42] X. Chen, K. H. Burrell, N. M. Ferraro, T. H. Osborne, M. E. Austin, A. M. Garofalo, R. J. Groebner, G. J. Kramer, N. C. Luhmann, and G. R. McKee, Rotational shear effects on edge harmonic oscillations in DIII-D quiescent H-mode discharges, Nucl. Fusion **56**, 076011 (2016).

[43] R. J. Colchin, D. L. Hillis, R. Maingi, C. C. Klepper, and N. H. Brooks, The filterscope, Rev. Sci. Instrum. **74**, 2068 (2003).

[44] T. N. Carlstrom, G. L. Campbell, J. C. DeBoo, R. Evanko, J. Evans, C. M. Greenfield, J. Haskovec, C. L. Hsieh, E. McKee, R. T. Snider *et al.*, Design and operation of the multipulse Thomson scattering diagnostic on DIII-D, Rev. Sci. Instrum. **63**, 4901 (1992).

[45] Ch. P. Ritz, E. J. Powers, and R. D. Bengtson, Experimental measurement of three-wave coupling and energy cascading, Phys. Fluids B **1**, 153 (1989).

[46] S.-I. Itoh, K. Itoh, Y. Nagashima, and Y. Kosuga, On the application of cross bispectrum and cross bicoherence, Plasma Fusion Res. **12**, 1101003 (2017).

[47] R. A. Haubrich, Earth noise, 5 to 500 millicycles per second: 1. Spectral stationarity, normality, and nonlinearity, J. Geophys. Res. **70**, 1415 (1965).

[48] S. Elgar and R. T. Guza, Statistics of bicoherence, IEEE Trans. Acoust. Speech Signal Process. **36**, 1667 (1988).

[49] S. Elgar and G. Sebert, Statistics of bicoherence and biphase, J. Geophys. Res. **94**, 10993 (1989).

[50] M. A. Van Zeeland, R. L. Boivin, T. N. Carlstrom, T. Deterly, and D. K. Finkenthal, Fiber optic two-color vibration compensated interferometer for plasma density measurements, Rev. Sci. Instrum. **77**, 10F325 (2006).

[51] R. J. La Haye, S. Günter, D. A. Humphreys, J. Lohr, T. C. Luce, M. E. Maraschek, C. C. Petty, R. Prater, J. T. Scoville, and E. J. Strait, Control of neoclassical tearing modes in DIII-D, Phys. Plasmas **9**, 2051 (2002).

[52] T. A. Casper, K. H. Burrell, E. J. Doyle, P. Gohil, C. J. Lasnier, A. W. Leonard, J. M. Moller, T. H. Osborne, P. B. Snyder, and D. M. Thomas, Density and temperature profile modifications with electron cyclotron power injection in quiescent double barrier discharges on DIII-D, Plasma Phys. Controlled Fusion **48**, A35 (2006).

[53] N. J. Richner, L. Bardóczi, J. D. Callen, R. J. La Haye, N. C. Logan, and E. J. Strait, Use of differential plasma rotation to prevent disruptive tearing mode onset from 3-wave coupling, Nucl. Fusion **64**, 106036 (2024).

[54] L. L. Lao, J. R. Ferron, R. J. Groebner, W. Howl, H. St. John, E. J. Strait, and T. S. Taylor, Equilibrium analysis of current profiles in tokamaks, Nucl. Fusion **30**, 1035 (1990).

[55] O. Meneghini and L. Lao, Integrated modeling of tokamak experiments with OMFIT, Plasma Fusion Res. **8**, 2403009 (2013).

End Matter

Symmetries in the bispectrum related to interchanging the order of indices and $F(-f) = F^*(f)$ imply equivalent bicoherence should (and does) appear at $(51, -17)$ and $(51, -34)$ kHz. We therefore include the negative frequency space to highlight symmetry in the bicoherence. Figure 5 shows the bicoherence, calculated from RIP data and including negative frequency space, for each frequency pair (f_1, f_2) with $f_3 = f_1 + f_2$. As in Fig. 2(b), the ensemble contains 1400 time segments of length 0.5 ms. Figures 6 and 7 provide the same data for an outboard midplane sensing coil and BES channel viewing the outboard midplane at $\rho = 0.92$, respectively, also including negative frequency space. As in the RIP data, both demonstrate bicoherence at (34,17) kHz above the 99% significance level.

Figure 8 shows a cross-sectional diagram of DIII-D, with the locations of the three diagnostics employed in this Letter marked. BES views the area shown.

Figure 9 shows the results of convergence tests for the bicoherence at (34,17) kHz (the frequencies of the EHO harmonics) for RIP data, sensing coil data, and BES data. The ensemble sample size N is varied by segmenting the full data records from 1100 to 1800 ms. The frequency resolution is, therefore, the least at the largest N. The bicoherence for RIP data decreases somewhat at large N for two reasons: (i) The coherent mode energy is distributed across multiple frequency bins, and (ii) uncorrelated noise spreads into the bins associated with the mode. The sensing coil and BES have smaller noise, evident in Fig. 1.

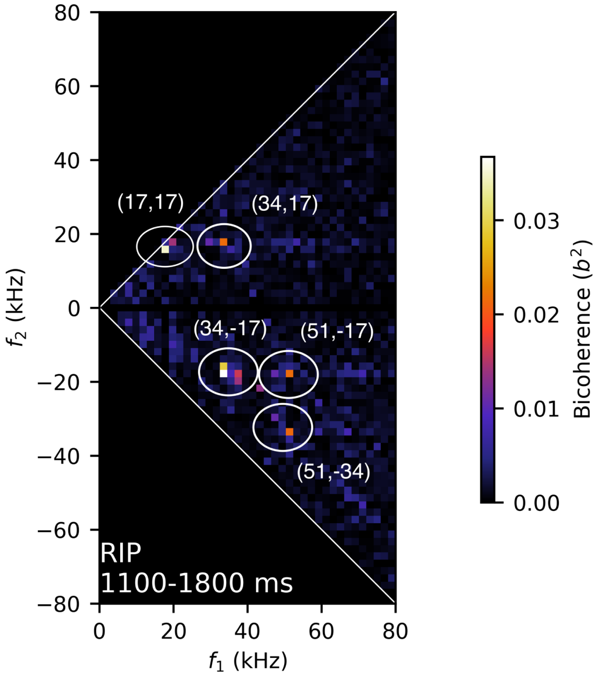

FIG. 5. From data in Fig. 1(a), bicoherence in RIP data averaged from 1100 to 1800 ms.

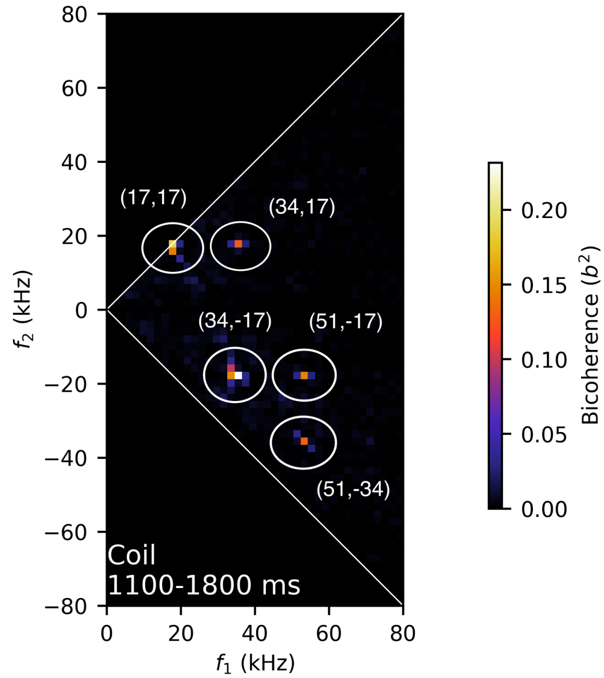

FIG. 6. From data in Fig. 1(b), bicoherence in sensing coil data averaged from 1100 to 1800 ms.

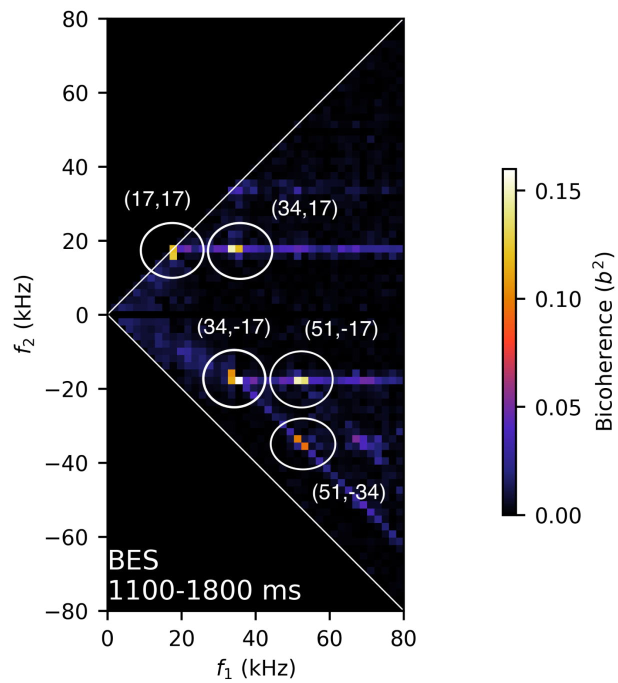

FIG. 7. From data in Fig. 1(c), bicoherence in BES midplane $\rho = 0.92$ data averaged from 1100 to 1800 ms.

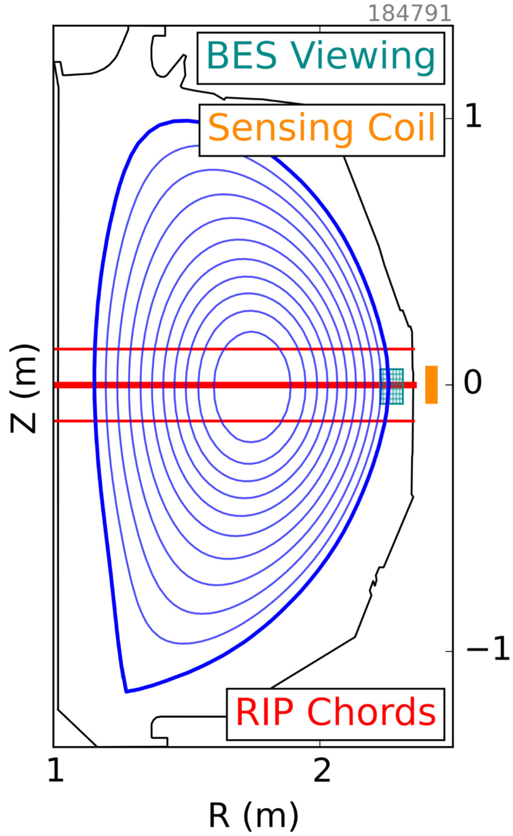

FIG. 8. A diagram of the locations of RIP (red), the relevant sensing coil (orange), and the viewing area of BES (cyan) on DIII-D in shot 184791. RIP $Z = 0$ chord marked with a thicker line. Flux surfaces are marked in blue. BES is located at a toroidal azimuth of 150°, RIP at 285°, and the low-noise sensing coil at 322° in machine coordinates.

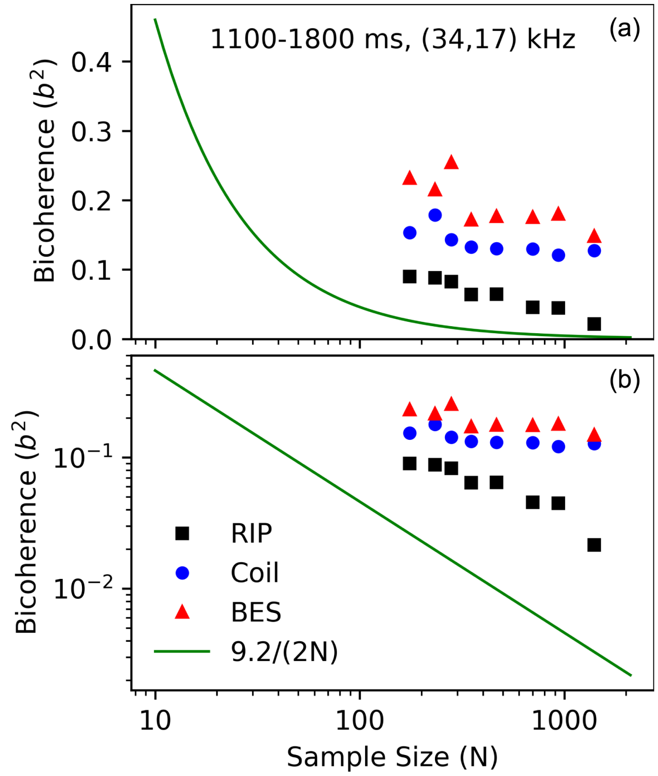

FIG. 9. (a) Bicoherence values for RIP (black squares), sensing coil (blue circles), and BES (red triangles) data at (34,17) kHz as the ensemble sample size is increased from $N = 175$ to $N = 1400$. The green curve is the 99% significance level $9.2/(2N)$. (b) The same quantities on a logarithmic scale in b^2.